

RESEARCH ARTICLE

Experimental investigation of an optimized airfoil for vertical-axis wind turbines

Daniele Ragni, Carlos Simão Ferreira and Giuseppe Correale

Delft University of Technology, Delft, The Netherlands

ABSTRACT

The present study addresses the experimental verification of the performance of a new airfoil design for lift-driven vertical-axis wind turbines (VAWTs). The airfoil is obtained through a genetic-algorithm optimization of an objective function which maximizes the aerodynamic performance of airfoils having a larger thickness, providing better structural stiffness compared to more slender NACA design. The work presents an experimental analysis of such improved performance of a 26% thick VAWT-optimized airfoil (DU12W262). The 2D flow velocity, pressure and aerodynamic loads are measured by combined use of particle image velocimetry, wall-pressure sensors and wake rakes. Additionally, the airfoil surface pressure is determined by integrating the pressure equation from the experimental velocity field. Results are initially obtained with the airfoil in steady conditions, at Reynolds 3.5×10^5 , 7.0×10^5 and 1.0×10^6 with both free and forced (1% c) boundary layer transition. Xfoil simulations are employed for comparison with the experimental results, showing a good agreement in the linear range of angle of attack and a consistent lift/drag overestimation in the separated one. The airfoil performance is further assessed under pitching conditions (oscillatory, ramp up), at Reynolds 7.0×10^5 with reduced frequencies ranging from 0.07 to 0.11 and the aerodynamic load behaviour compared with the steady case. The experimental data are used as input for a numerical simulation of a 2D VAWT; while the performance are compared with those for NACA 4-series airfoils commonly used for VAWTs, showing a significantly higher maximum power coefficient for the optimized airfoil. All the data presented in the manuscript are made available in the Supporting information. Copyright © 2014 John Wiley & Sons, Ltd.

KEYWORDS

VAWT vertical axis wind turbine; airfoil design optimization; load determination; lift; drag; particle image velocimetry

Correspondence

Daniele Ragni, Wind Energy Section, Kluyverweg 1, 2629 HS Delft, The Netherlands.

E-mail: D.Ragni@tudelft.nl

Received 12 June 2013; Revised 4 January 2014; Accepted 6 June 2014

1. INTRODUCTION

Recent developments in offshore wind energy renewed the interest in the performance of lift-driven vertical-axis wind-turbines (VAWTs), with particular attention to floating installations (Akimoto *et al.*,¹ Paquette and Barone,² Paulsen *et al.*,³ Sutherland *et al.*,⁴ Jamieson⁵). VAWTs experience complex aerodynamics at blade, rotor and wind-farm scales, which directly influence the cost of energy. An optimal compromise between aerodynamic performance and structural stiffness requires a multi-scale optimization, including the blade, the rotor and the wind-farm scales. In the past decades, VAWT blades have typically been designed with symmetric airfoils, most often NACA 4-digit family, in particular the NACA0012, NACA0015 and NACA0018 (Sheldahl and Klimas⁶ and Timmer⁷). Among past research into the design and testing of VAWTs airfoils stands out the research developed at the Sandia National Laboratories (Klimas⁸) and at the Glasgow University (Galbraith *et al.*⁹), primarily focusing on the steady and pitching performance of families of cambered airfoils, together with the studies at the Delft University of Technology for small-scale VAWTs applications VAWTs (Claessens¹⁰). The research at Sandia National Laboratories and at the Glasgow University achieved two milestones: the determination of desirable section characteristics for lowering the cost of energy;⁸ and the coupling of the airfoil design optimization with a vorticity-based model of the rotor,⁹ eliminating several of the incorrect assumptions of stream-tube models. The work of Klimas,⁸ citing the work of Sullivan,¹¹ includes as design drivers the impact of stall regulation in thin airfoils (*modest values of maximum lift coefficient with relatively sharp stall*,⁸) together with the obvious reduction of airfoil drag

(low zero lift drag coefficients, and [...] wide drag buckets, Klimas⁸). The work of Galbraith *et al.*⁹ integrates and extends the improvements at the airfoil scale in the modelling of the induction field developed by Jiang *et al.*¹² (see also Basuno *et al.*¹³ and Coton *et al.*¹⁴). One of the main disadvantages of the usage of thin airfoils in VAWTs is their reduced structural stiffness, leading to an increased blade mass. The use of thin airfoils is the result of using the airfoil's glide ratio $\frac{c_l}{c_d}$ as the design guideline. The work of Simão Ferreira and Geurts,¹⁵ following the work of Wilson,¹⁶ Coene,¹⁷ Madsen,^{18,19} Simão Ferreira²⁰ and Simão Ferreira and Scheurich²¹ (see also Jamieson⁵), presents instead an objective function for the aerodynamic optimization of VAWTs airfoils based on the first principle of the 2D VAWT aerodynamics. In particular, the generation of the wake by variation of the bound circulation on the airfoil and the dependency of the latter with solidity and airfoil lift slope is used as a guideline to the design. The derivation of the function demonstrates that high aerodynamic performance can be obtained with thicker airfoils, since airfoil lift slope is proportional to its thickness (in the linear region of the lift slope). In the present study, a new airfoil is designed from the optimization procedure according to Simão Ferreira and Geurts.¹⁵ From the procedure that allows obtaining a thicker airfoil with good aerodynamic performance, the manuscript focuses on an experimental investigation to validate the simulated airfoil lift and drag performance. The present study is structured in four main sections:

- Section 2—design and optimization of an airfoil (DU12W262) according to Simão Ferreira and Geurts,¹⁵ for tip speed ratio $\lambda = \frac{\Omega R}{U_\infty} > 5$.
- Sections 3, 4 and 5—experimental validation by combined use of particle image velocimetry (PIV), wall pressure probes and wake rake data on an experimental model of the DU12W262 airfoil, tested at the low-turbulence wind tunnel of Delft University of Technology for several Reynolds numbers $3.5 * 10^5$, $7.0 * 10^5$ and $1.0 * 10^6$. The measurements include steady conditions (both free transition and forced transition at the leading edge) and unsteady measurements for pitching motions.
- Section 6—simulation of the performance of a VAWT using the experimental data from Section 5.
- Section 7—conclusions and future work.

2. DESIGN OF THE DU12W262 AIRFOIL

The DU12W262 airfoil shape is the result of an optimization for aerodynamic and structural performance (Simão Ferreira and Geurts.¹⁵ Selected from an initial population of airfoils through a genetic algorithm, the shape is evaluated via two objective functions. The optimization algorithm used in this work was developed by de Oliveira²² and Simão Ferreira and Geurts;¹⁵ it is constructed around the NSGA-II algorithm as implemented in MATLAB R2011. The most relevant elements of the algorithm are described by de Oliveira.²² The structural objective function was defined as the bending stiffness in flap-wise direction of the airfoil per wall thickness, in reference to the centroid of the airfoil. The aerodynamic function is the one presented by Simão Ferreira and Geurts.¹⁵ The first simplification relates to the range and distribution of angles of attack over the turbine revolution. The range of angles of attack will vary for different tip-speed ratios and different values of $\frac{3c}{2R}$ (assuming rigid, fixed pitch blades); in the present study, a single evaluation interval of angles of attack ($\Delta\alpha = 14^\circ$) is accounted for in a range of possible angles of attack $-20^\circ < \alpha < 20^\circ$. The function is given by equation (1), where

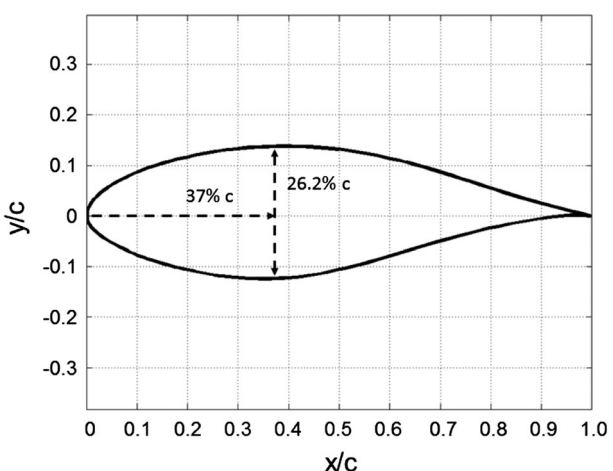


Figure 1. DU12W262 airfoil geometry.

$b(\alpha)$ is a weighting function based on the angles of attack distribution presented in Simão Ferreira and Geurts.¹⁵ Any variation of dynamic pressure with the azimuthal position is not taken into account, because of the lower impact shown in a secondary analysis, where it was found that the dynamic pressure variations mostly average out across leeward and windward regions.

$$F_{aero} = -\max \left(\left(\frac{\int_{\chi}^{\chi+\Delta\alpha_r} c_{l\alpha} d\alpha}{\int_{\chi}^{\chi+\Delta\alpha_r} c_d b(\alpha) d\alpha} \right), \text{ for all values of } \chi, \text{ with } -20^\circ < \chi < 5^\circ \right) \quad (1)$$

where $c_{l\alpha}$ and c_d are the lift slope and drag coefficient as a function of angle of attack α . The optimized airfoil generation produces geometrical shapes with a wide range of thicknesses, among which the one with $t/c = 26.2\%$ was chosen. The resulting DU12W262 airfoil is presented in Figure 1, and the airfoil coordinates are given in Appendix.

3. EXPERIMENTAL SETUP

3.1. Airfoil realization and wind tunnel measurements

The DU12W262 airfoil shape has been manufactured into an aluminium model of chord $c = 0.25$ m, span $s = 1.25$ m, aspect ratio $AR = s/c = 5$ and thickness $t/c = 26.2\%$, with a mass of 34.7 kg. The model has been vertically installed in the closed-circuit low-turbulence wind tunnel (LTT) of the TU Delft laboratories, in an octagonal test section 1.80 m wide, 1.25 m high and 2.60 m long, resulting in a blockage ratio from 3.6% to 4.7% in the range from -20° to 20° angles of attack. With a contraction ratio of 17.6, the wind tunnel can reach a maximum wind speed of 120 m s $^{-1}$ and a turbulence level ranging within 0.015% to 0.07% with wind speeds from 10 to 75 m s $^{-1}$ (from hot wire anemometry profiles with low-pass filter at 50 kHz). In Figure 2 (left), an image of the model installed in the test section is presented. The airfoil model has been supported from the top by combined use of an SKF axial and a radial bearing, while at the bottom, it was fitted through a radial bearing into a Plexiglas window.

An electromagnetic linear actuator with a digital controller (Compax3 C3 S025 V2 F10I10T10M00) was used to control the pitching motion of the airfoil, able to deliver a constant/peak forces of 300/600 N. The maximum pitching frequency is 3 Hz at $\pm 10^\circ$ oscillation amplitude, dropping to 2 Hz with $\pm 20^\circ$ amplitude. The linear motion has been transformed into a pitching one by use of an aluminium connection provided with two bearings (Figure 2-right). The mechanism has been connected to the aerodynamic centre of the airfoil to minimize the effect of the aerodynamic moments reacting on the actuator. Steady-flow measurements have been performed by acquiring several angles of attack at Reynolds $3.5 * 10^5$, $7.0 * 10^5$ and 10^6 , with wind-tunnel speeds ranging from 20 to 60 m s $^{-1}$. Pitching tests have been performed at a Reynolds number of $7.0 * 10^5$, for respectively $\pm 5^\circ$, $\pm 10^\circ$, $\pm 20^\circ$ amplitude variation, with reduced frequencies ranging from $k = 0.07$ to $k = 0.11$. The obtained cycle shapes result from the linear actuator imposing a quasi-linear acceleration/deceleration on the actuating rod. The obtained shape profiles, though not sinusoidal, allowed for a better response of the system to vibrations and a lower inertial force effect on the wind-tunnel walls.

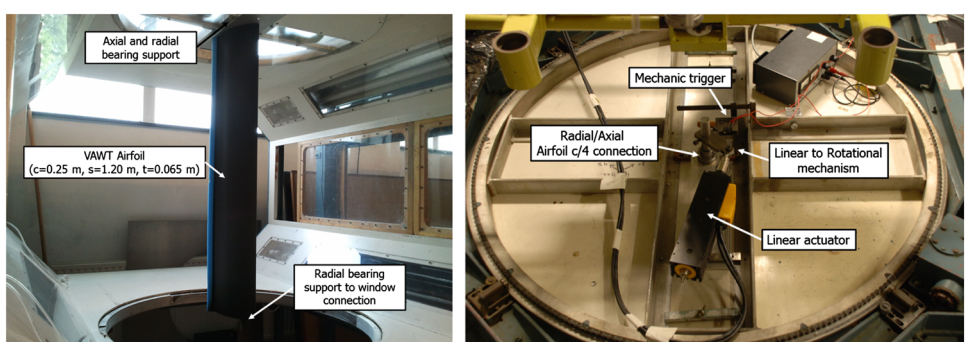


Figure 2. Installation of the DU12W262 airfoil in the wind-tunnel test section (left), electromagnetic actuator for the pitching movement (right).

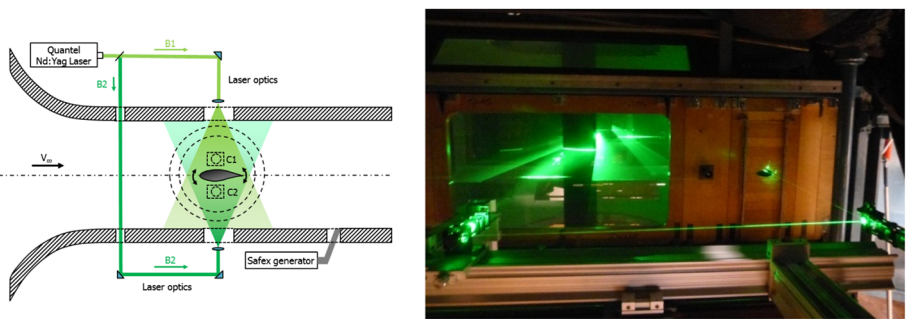


Figure 3. Top view of the PIV apparatus (left), B1 B2: illumination beams, C1 C2 cameras; realization of the PIV setup (right).

3.2. PIV diagnostic apparatus

The flow velocity fields at different angles of attack have been obtained by performing 2D double-camera PIV measurements. The velocity results have been used to compute pressure and aerodynamic loads for both steady and pitching configurations (van Oudheusden *et al.*,²³ Ragni *et al.*²⁴). Seeding particles have been produced by a SAFEX fog machine able to generate droplets with a median diameter of $\approx 1\mu\text{m}$. The seeding particles have been injected downstream of the model, determining a uniform and homogeneous concentration at the test section after flow recirculation in the closed circuit. Laser illumination is provided at the airfoil middle-span by a Quantel CFR200 Nd:YAG laser (200 mJ per pulse) and conveyed through laser optics to form a laser sheet of approximately 2 mm thickness at the field of view (FOV). In both steady and pitching conditions, a double-sided illumination setup has been used in order to reduce the effect of laser shadow (Figure 3). The double-sided illumination has been obtained by splitting the laser beam into two beams (B1, B2 in Figure 3) through a cubical beam splitter. Two CCD LaVision Imager Pro LX cameras of $4872 \times 3248 \text{ pix}^2$ with two Nikon lenses of 105 mm focal length and aperture f#5.6 are combined to form a planar FOV encompassing the airfoil shape and perpendicular to the span-wise direction (section plane). Additionally, the usage of two cameras allow seeing both top and bottom airfoil surfaces, mitigating the prospective effect encountered with just one camera. Image acquisition and processing has been carried out by LaVision DaVis 8.1 software. For each angle of attack, approximately 200 images have been captured and processed by average correlation, with a window size of $24 \times 24 \text{ pix}^2$ and 50% overlap, giving a vector spacing of 0.9 mm. The images have been combined into a single FOV encompassing the airfoil. In the pitching configuration, the same setup has been employed; the acquisition has been synchronized with the phase of the pitching motion (phase-locked) through the use of a Stanford acquisition system and a mechanical trigger installed on the pitching axis.

Different PIV velocity fields have been acquired to visualize the flow and to obtain the forces to be compared with the pressure sensors (wall-tunnel pressure probes and wake rake Pitot tubes).

4. PRESSURE AND LOAD DETERMINATION METHODOLOGY

The aerodynamic loads are obtained for both steady and pitching configurations. In the steady airfoil configuration, a series of 44 (22 per wall, variable spacing from 17.8 to 4.5 cm, total length of 2.095 m) wind-tunnel wall-pressure orifices have been employed to obtain the static pressure distribution on the wind-tunnel mid-span. Additionally, a wake rake constituted of 64 Pitot probes (variable spacing from 3 to 24 mm, total length of 0.516 m) has been employed to measure drag at the different angles of attack. In both pitching and steady airfoil configurations, the lift coefficient has been also obtained through the PIV load determination as in Ragni *et al.*²⁴ Several studies already demonstrated that the PIV load estimation procedure usually determines drag values with higher inaccuracies than the lift ones, because of the small momentum imbalance to be captured by PIV in the wake (van Oudheusden *et al.*,²³ van Oudheusden²⁵). In the present analysis, the more accurate wake rake results have been used for the determination of the drag force for the steady case. Because of the relatively slow response of the wake rake (within 0.5 Hz), no drag measurements were completed for the unsteady configuration. The pressure field is directly derived from the PIV velocity fields. Except for the airfoil boundary layer and for the airfoil wake, the flow is potential; therefore, the Bernoulli equation can be used to directly evaluate the pressure coefficient c_p from the local velocity $V \text{ m s}^{-1}$ and the free stream one $V_\infty \text{ m s}^{-1}$ at the boundary of the FOV (except wake):

$$c_p = 1 - \left(\frac{|\bar{V}|}{V_\infty} \right)^2 \quad (2)$$

In the airfoil wake, the flow is viscous, and the Bernoulli equation is not valid; therefore, the pressure is computed from the integration of the Navier–Stokes pressure gradient:

$$\frac{\bar{\nabla}p}{p} = -\rho \left(\frac{\partial \bar{V}}{\partial t} + \bar{V} \cdot \bar{\nabla} \bar{V} \right) + \bar{\nabla} \bar{\tau} \quad (3)$$

The velocity time derivative term is evaluated from PIV velocity fields obtained at consecutive phases (Ragni *et al.*²⁴). The pressure distribution is obtained by rewriting equation (3) in the Poisson form and integrated in 2D by a second-order finite difference scheme, imposing Dirichlet–Bernoulli conditions on the outer boundary of the flow (free-stream), and Neumann boundary conditions on the wake boundary (Ragni *et al.*²⁴). Viscous and Reynolds turbulent stresses have been included in the formulation, even though from the data evaluation, their contribution is found to be negligible for the lift derivation, confirming previous results (van Oudheusden *et al.*²³). By integrating the momentum change in the flow, the force acting on the body can be derived from its reaction on the flow.

4.1. Uncertainty analysis

The velocity vectors obtained from PIV possess random error and bias. In the present steady airfoil configuration, as shown in Table I, the errors on the PIV field derived by ensemble correlation have a statistical convergence that scales with $1/\sqrt{N}$, where N equals 200 in this study. In a typical planar PIV setup, where the correlation uncertainty is estimated of the order of 0.1 px [Westerweel²⁶], assuming a free-stream particle displacement of 15 px and a reference wind-speed of 40 m s^{-1} , the expected uncertainties in the velocity vector amount to 0.26 m s^{-1} for the instantaneous snapshots and to 0.02 m s^{-1} for the mean values. The presence of random velocity fluctuations on the mean values varies within the field, from regions of 0.7% in the free-stream up to 50% fluctuations in the separated boundary layer at $+20^\circ$ angle of attack at Reynolds 10^6 . With the current optical setup, and the given the resolution of 0.9 mm, the expected unresolved higher fluctuations levels are of the order of 8.7 m s^{-1} encountered at $+10^\circ$ angle of attack at Reynolds 10^6 . On the other side, the minimum fluctuations observed in the free-stream flow are of the order of 0.30 m s^{-1} at Reynolds $7.0 * 10^5$ (0.7% of the free-stream), much higher than what was expected from the turbulence value of the wind tunnel. Using these values as reference, the overall uncertainty on the mean velocity due to the random components is assessed at 0.62 m s^{-1} for the steady case and 0.82 m s^{-1} for the pitching case (because of the lower free-stream velocity). Most of the relevant systematic sources of uncertainties (Elsinga *et al.*²⁷ Schrijer and Scarano²⁸) discussed in previous high-speed airfoil applications have here a low impact due to the lower acceleration in the flow and to the relaxation time of the SAFEX fog, estimated to be below $1 \mu\text{s}$. The evaluation of the uncertainty on the spatial resolution is typically challenging. In the present analysis, the resolution plays an important role for the evaluation of the airfoil surface pressure. Through an *a posteriori* evaluation of the wake thickness, determined by a turbulent Karman vortex shedding (typical vortex size 8 mm), together with an in-plane resolution of 1.8 mm (corresponding to a window size of $24 * 24$ with 50% overlap), the normalized window size ws/λ of 0.16 can be converted into a velocity error of < 4% (Schrijer and Scarano²⁹). The error due to peak-locking constitute the main error due to the large FOV encompassed at the relatively low aperture number. Quantification by statistical analysis on the histograms of the difference between the velocity measured and its rounded off values (Ragni *et al.*²⁴) estimates the peak-locking velocity error to 0.05 px corresponding to a velocity of 0.13 m s^{-1} . Calculation of the pressure requires estimating the error on pressure and loads. In regions of negligible vorticity, the steady Bernoulli equation can be used to retrieve pressure. In these regions, the error is a function of the velocity error; therefore, with an estimated velocity error of $1.72\text{--}1.80 \text{ m s}^{-1}$ obtained from the velocity contributions, the error on the pressure can be estimated from a linear propagation analysis of equation (2). The estimation gives for the pressure an uncertainty of 0.08–0.09 for the steady and pitching cases. The pressure in the vortical regions is obtained from integration of the 3D momentum equation, by a second-order Poisson algorithm with potential boundary conditions;²⁴ because of the relatively well-resolved velocity fields, the pressure solver keeps the uncertainty on the pressure of the order of the Bernoulli values, on the basis of the

Table I. Summary of the estimated uncertainty values.

	Uncertainty	Reference	Steady airfoil values	Pitching airfoil values
Velocity	Correlation	$\varepsilon = 0.1 \text{ px}$	0.02 m s^{-1}	0.03 m s^{-1}
	Statistical fluctuations	$\sigma_{ref} = 8.78 \text{ m s}^{-1}$	0.62 m s^{-1}	0.82 m s^{-1}
	Spatial resolution	$ws/\lambda = 0.23$	1.60 m s^{-1}	1.60 m s^{-1}
	Peak locking	$l_\varepsilon = 0.05\text{--}0.07$	0.13 m s^{-1}	0.18 m s^{-1}
Loads	Pressure coefficient	$f\{c_p(\bar{V})\} * \varepsilon_V$	0.08	0.09
	Lift coefficient	$\sigma_{contours}$	0.005	0.005
	Angle of attack	$\Delta\alpha$	0.01°	0.05°

velocity. In order to give an indication of the uncertainty on the loads, two main inaccuracy aspects have to be quantified: an uncertainty on the angle of attack and on the value. While in the steady configuration, the uncertainty on the angle of attack is below 0.01 deg because of the direct connection to the tunnel angle actuator, the value increases to 0.05 when considering the pitching angles, because of the jittering of the triggering devices. The uncertainty on the force values depends upon the combination of the previous sources of inaccuracy in the contour approach. Therefore, the standard deviation resulting from choosing different surface boundary contours for the PIV load integration is assumed as a quantification of the uncertainties on the experimental forces. In fact, the integration via the momentum conservation law is theoretically independent of the contour shape and dimension, while the integration of the PIV data includes the combination of the single uncertainties values in the force value. The standard deviations of the lift coefficients as obtained from the contour approach is of 0.005 obtained from 20 different contour in the field.

5. EXPERIMENTAL RESULTS

5.1. Steady airfoil results

The results for steady flow are obtained for different angles of attack ranging from -20° to $+20^\circ$ are acquired at two Reynolds numbers $Re = 10^6$ and $Re = 7 * 10^5$. The results for five angles of attack (ensemble averaged results) are presented: normalized velocity field (Figure 4), normalized vorticity field (Figure 5) and pressure field (Figure 6).

The velocity contours in Figure 4 pertain to the airfoil in steady conditions and free transition at Reynolds 10^6 and show the variations of the airfoil flow features along the tested angles of attack. The separation at positive pitched angles occurs on the suction side at $+10^\circ$ at about 65% chord, while at -10° , the airfoil maintains attached flow until 70% chord of the bottom surface (suction side negative angles). The airfoil camber results in a variation of the lift coefficient of more than 20% when comparing positive and negative stall angles. The computation of the pressure coefficient through PIV is usually a delicate procedure (Ragni *et al.*²⁴), because of the effect of reflection, seeding response and optical aberrations. In the present analysis, the previous sources have a lower impact because of the double-sided illumination that reduces the effect of illumination and to the lower acceleration. The pressure computation (Figures 7 and 8) for Reynolds $1.0 \cdot 10^6$ and $0.7 \cdot 10^6$ shows the evolution of the pressure coefficient along the suction and pressure side, in comparison with data reproduced

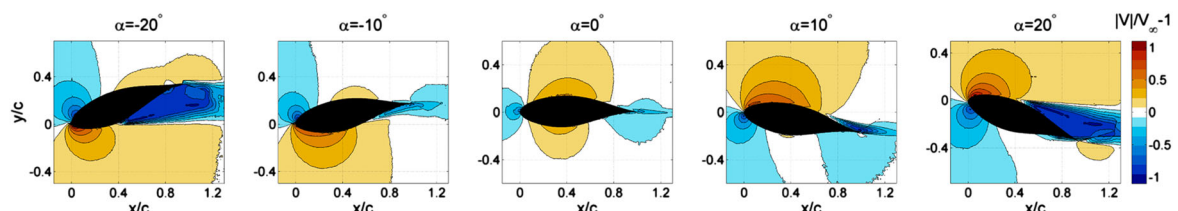


Figure 4. PIV normalized velocity magnitude (free-stream reference), steady airfoil configuration, free transition, $Re = 10^6$.

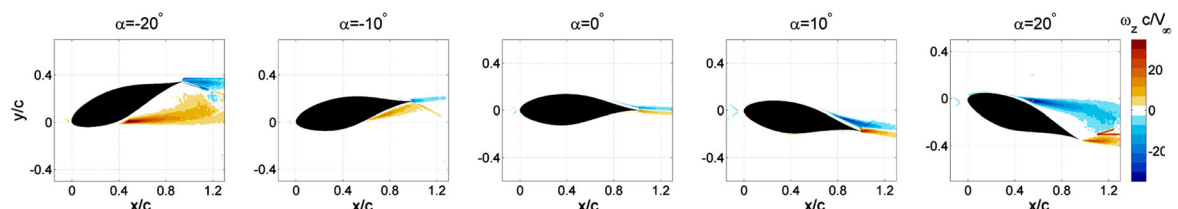


Figure 5. PIV normalized vorticity magnitude, steady airfoil configuration, free transition, $Re = 10^6$.

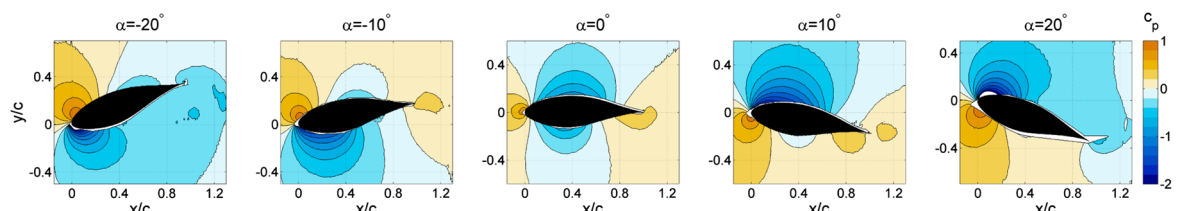


Figure 6. PIV pressure coefficient, steady airfoil configuration, free transition, $Re = 10^6$.

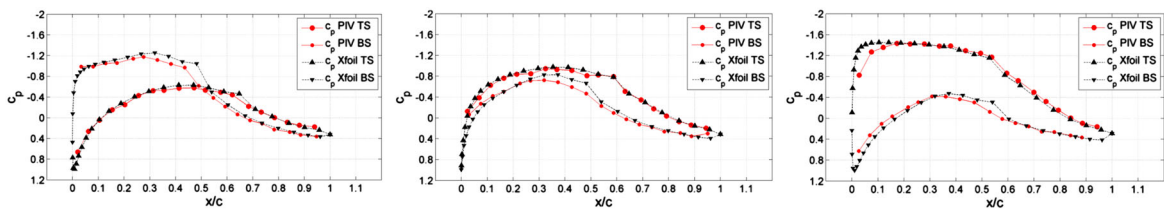


Figure 7. Pressure coefficient distribution pressure distribution for top (T) and bottom (B) airfoil surfaces (S), results from PIV integrated pressure, Xfoil, angles of attack -5° , 0° , $+5^\circ$, $Re = 1.0 \cdot 10^6$.

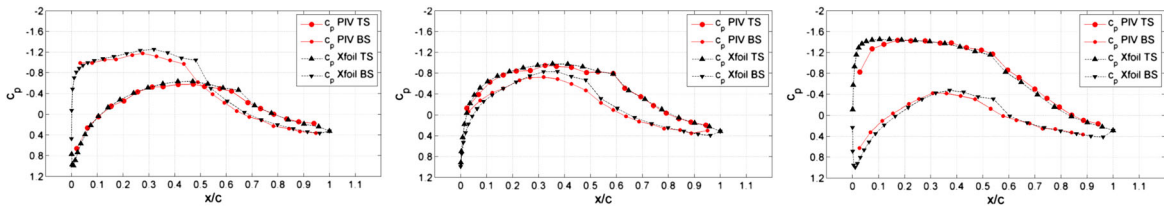


Figure 8. Pressure coefficient distribution pressure distribution for top (T) and bottom (B) airfoil surfaces (S), results from PIV integrated pressure, Xfoil, angles of attack -5° , 0° , $+5^\circ$, $Re = 0.7 \cdot 10^6$.

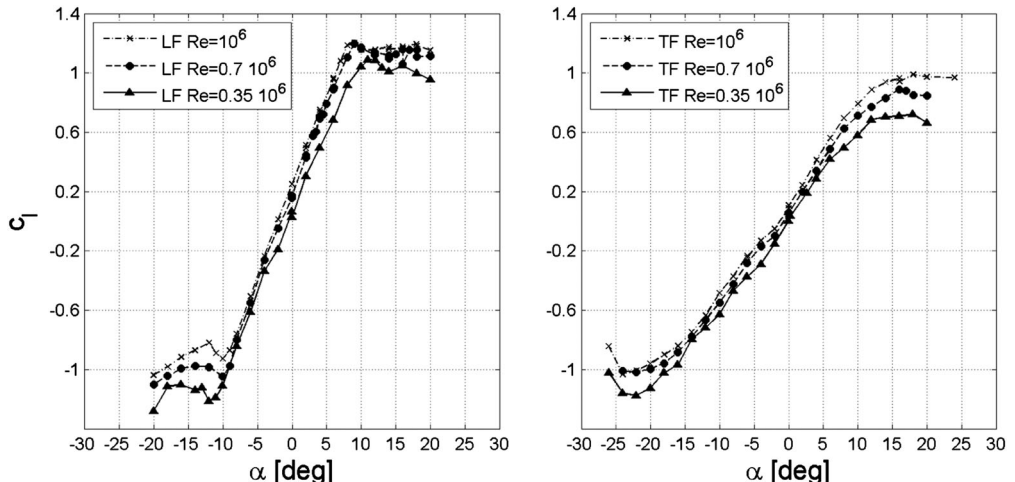


Figure 9. Lift coefficient (experimental) for the DU12W262 under free (left) and forced (right) transitions.

from Xfoil computations. Despite the effect of the laminar separation bubble, a good agreement is found a part from the closest region near the leading edge at $+5^\circ$ angle of attack, where the PIV underestimates the peak suction pressure as noticed already in previous similar studies (Ragni *et al.*²⁴). Further investigation is left to elucidate the role of the laminar bubble in the airfoil optimization procedure. It is supposed that the laminar separation bubble will allow for the wide drag bucket and thus the high lift-slope. In particular, it has been confirmed that the location of the laminar bubble does not vary significantly with angle of attack.

The variability of the airfoil performance with different Reynolds numbers has been investigated in more detail by use of the wind-tunnel wall-pressure sensors. Figure 9 presents the airfoil lift coefficients for different Reynolds numbers, in both free (left) and forced boundary layer transition (right) configurations as obtained from integration of the wind-tunnel wall-pressure. Figure 9 (left) shows a relatively low effect of the Reynolds number in the performance of the airfoil under free transition, mainly evidenced by a slight slope variation induced in the lift curve. With decreasing Reynolds number, a shift of the curve towards negative lift is noticeable. The configuration with forced transition in Figure 9 (right) presents a similar behaviour with the change in Reynolds number, although the effect of the fully turbulent flow in the airfoil delays stall to respectively $+15^\circ$ and -20° angles of attack, in comparison with $+10^\circ$, -12° in the clean configuration. These results are the consequence of the presence of a laminar separation bubble in the free transition case, which is no longer present in the forced transition configuration. The maximum lift coefficient at $Re > 7 \cdot 10^5$ is also reduced from the free to the forced transition configuration, decreasing from 1.2 to 0.95. The drag curves in Figure 10 are obtained with the wake

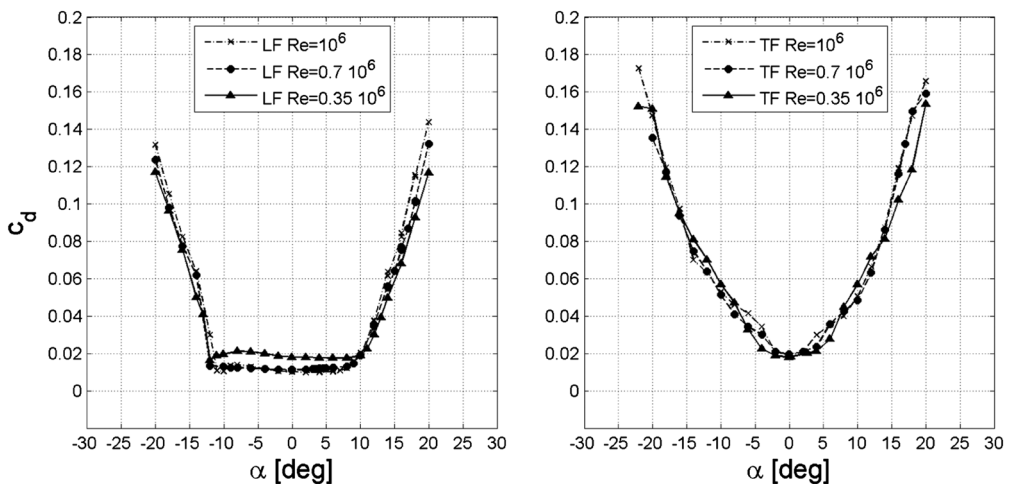


Figure 10. Drag coefficient (experimental) for the DU12W262 under free (left) and forced (right) transitions.

rake-installed downstream of the airfoil. The results in Figure 10 further confirms the effect of the change in Reynolds number in the airfoil under free and forced transition. The drag coefficient in the free transition configuration persists at an almost constant value in the attached flow range of angles of attack $+10^\circ$, -12° (cf. Figure 10), while in the forced transition, the range restricts to half.

The performance of the airfoil has been subsequently compared with the results obtained by Xfoil simulations. In particular, Figure 11 (top left) shows the lift coefficient distribution integrated from the velocity data compared with the one obtained by integration of the wind-tunnel wall-pressure profile and Xfoil results. Concurrently, in Figure 11 (top right), the experimental drag coefficient is compared with the one obtained from the Xfoil simulations. Because of the usual lower accuracy of the drag coefficient as computed from PIV, the experimental results are here obtained from integration of the total pressure measured by a wake rake of Pitot tubes, installed at almost two chords downstream of the airfoil profile. Figure 11 shows the asymmetrical load distribution for positive and negative angles, with maximum lift obtained at $+9^\circ$, -10° . The Xfoil simulations agree for most of the range of angles, over-predicting lift for angles higher than $+10^\circ$. Few differences are noticeable for the two investigated Reynolds numbers, which are primarily detectable on the measured drag coefficient in Figure 11 (top-right). Similarly to the lift coefficient distribution, the drag coefficient shows typically higher values reported in the separated zones than in the Xfoil simulations, fact ascribed to the way the boundary layer transition is obtained in the experiment with respect to the Xfoil simulations. The calculations are further carried on for the forced transition test cases in Figure 11 (bottom) and compared again with the wall-pressure probes and to the wake rake results. The resulting curves here show a much higher over prediction of the experimental results compared with the Xfoil simulations. The forced transition is experimentally obtained through the use of zigzag tape of 0.4 mm thickness and 6 mm pitch and positioned at 2% chord. Although the height of the zigzag tape is in the height range specified by Braslow and Knox³⁰ (from 0.07 to 0.47 mm), the relatively high value might justify the discrepancies with the Xfoil simulations, especially in the separated region. Similarly, in the XFOIL simulation, the airfoil transition is imposed at 2% chord and the results computed. The airfoil sensitivity to the presence of fully turbulent flow is relevant, especially with respect to the free-transition case. No-hysteresis phenomena are noted in any of the steady change of angles of attack.

5.2. Unsteady results

The VAWTs with optimal tip speed ratio $\lambda > 4$ require low blade solidities (c/R), leading to quasi-steady airfoil aerodynamics; however, turbulence can still originate unsteadiness. The results in this section are for validation of unsteady aerodynamics models.

The airfoil shape has been tested in unsteady pitching (Figure 12). The pitching motion is enforced by an electromagnetic actuator. The actuator is operated at different motion frequencies v and different motion amplitudes, corresponding to pitching cycles in a range of angles of attack. Different unsteady cycles have been obtained by varying the reduced frequency $k = \frac{\omega_c}{2V_\infty}$ from 0.07 to 0.11, by both the changing wind-tunnel speed and the pitching frequency. The PIV flow fields are obtained through ensemble average of instantaneous fields at different phases of the motion. Velocity data are acquired for the ramp-up motion and presented as velocity and vorticity contours. The pressure coefficient is computed by use of the unsteady Navier-Stokes momentum equation, using velocity fields at different phases to

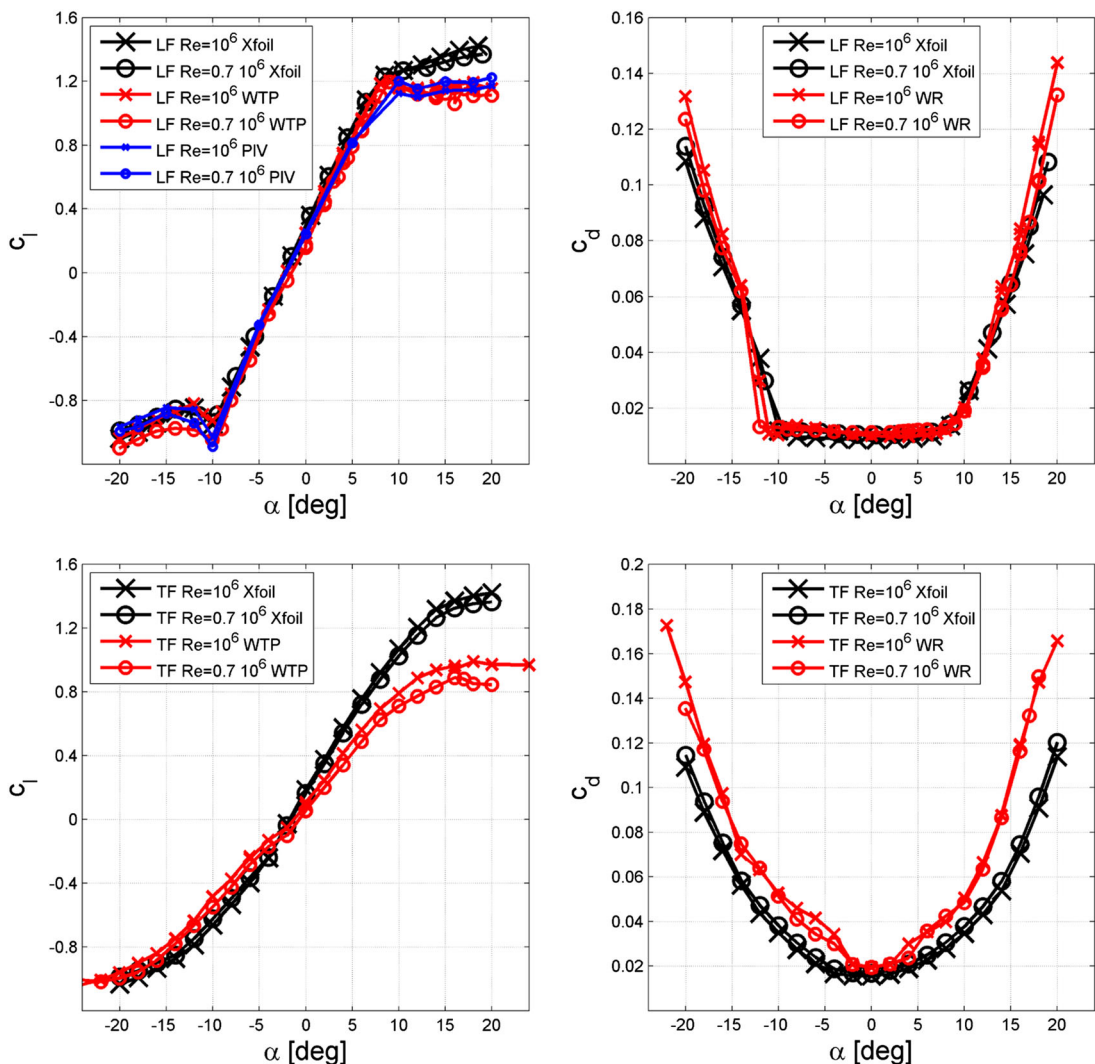


Figure 11. c_l and c_d obtained by tunnel pressure probes, wake rake, Xfoil simulations and from PIV load determination (free transition).

compute the time derivative. In the present section, the two main cases with $k = 0.07$ and $k = 0.11$ are discussed. The velocity profiles pertaining to the reduced frequency $k = 0.11$ in Figure 13 show few differences in the flow structures with respect to the steady case results, with the vorticity of the wake-convected downstream of the model. This is a notable result of the mutual effect of the airfoil thickness and the presence of the separation bubble, which mitigate the unsteady effects over the cycle. A lower suction of the airfoil is observed because of the ramp up of the airfoil that determines a lower circulation because of induction of the near wake. The present setup shows also its resolution limitations in representing the pressure peak at angles -8.3° and $+8.8^\circ$, as can be seen in proximity of the leading edge. These results are in agreement with unsteady airfoil theory, which predict a phase delay of bound circulation over the cycle (for the exception of two points). Figures 13, 14 and 15 present, respectively, the velocity magnitude, vorticity and pressure fields for several angles for the ramp-up part of the pitching motion for the case $k = 0.104$.

Figure 16 presents c_l versus angle of attack for the ramp-up part of the cycle of five pitching motions (different amplitudes, different reduced frequencies). The effect of the hysteresis is here visible in all cases; however, the relatively small size of the wake region compared with the airfoil potential flow suggests that the cause of the hysteresis is mainly dictated by the viscous effects of the developing boundary layer, rather than by the phase delay due to wake induction. In all five pitching motions, the minimum geometric angle of attack is near the static stall region, for which in the ramp-up region is an effect of the phase delay. This can be observed in the case of quasi-steady flow ($k = 0.028$), where the effect of loss

of lift at minimum measured angle of attack is largest because of the large amplitude of the pitching motion into highly separated flow region, despite the flow being quasi-steady.

5.3. Sensitivity to wind tunnel blockage and compressibility effects

The experimental results presented are not corrected for wind-tunnel blockage and compressibility effects. When applying the methodology for correction of experimental results of airfoil test at TU Delft's LTT, on the basis of the work of Allen³¹ and Acum *et al.*,³² the error in overestimation of lift slope is below 1.5% and below 1% in overestimation of drag.

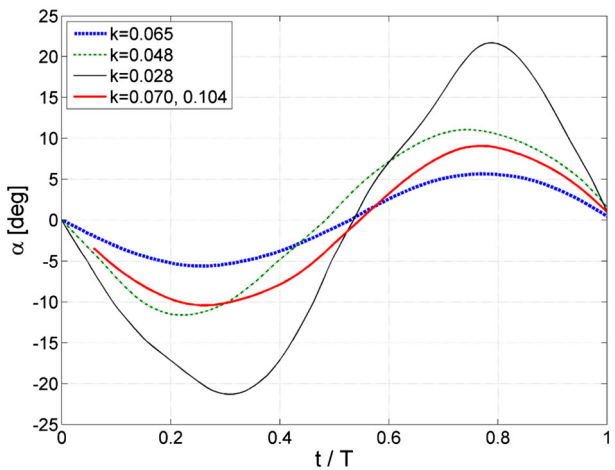


Figure 12. Cycles of actuation for the pitching airfoil.

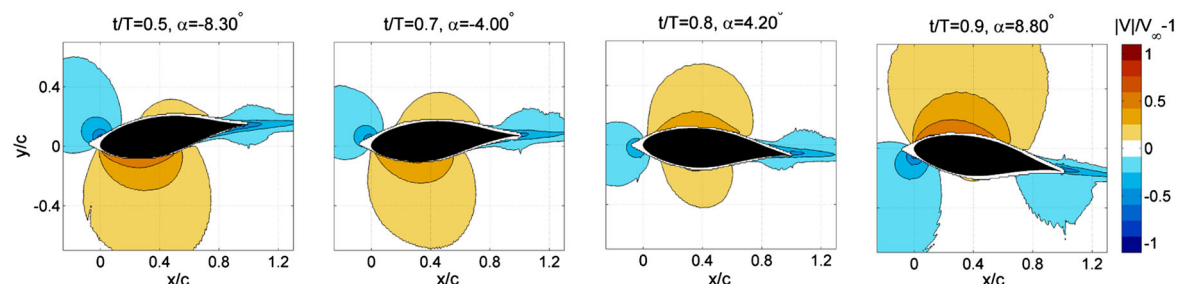


Figure 13. PIV normalized velocity magnitude (free-stream reference), pitching airfoil configuration, $k = 0.104$, $\nu = 2.66$ Hz, $V_\infty = 20 \text{ m s}^{-1}$.

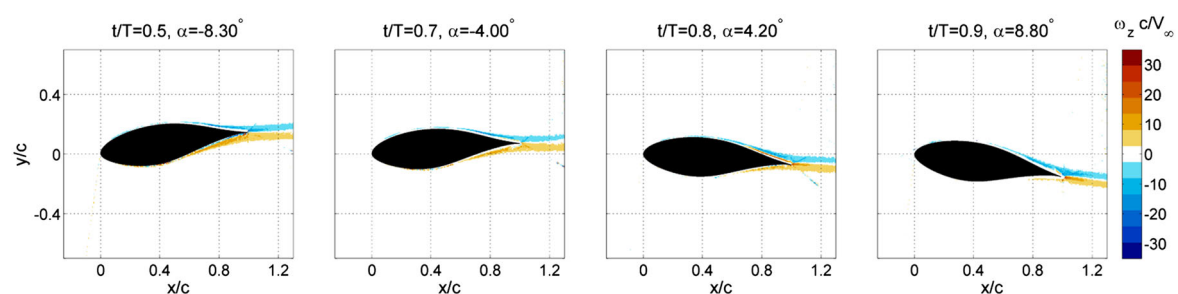


Figure 14. PIV normalized vorticity magnitude, pitching airfoil configuration, $k = 0.104$, $\nu = 2.66$ Hz, $V_\infty = 20 \text{ m s}^{-1}$.

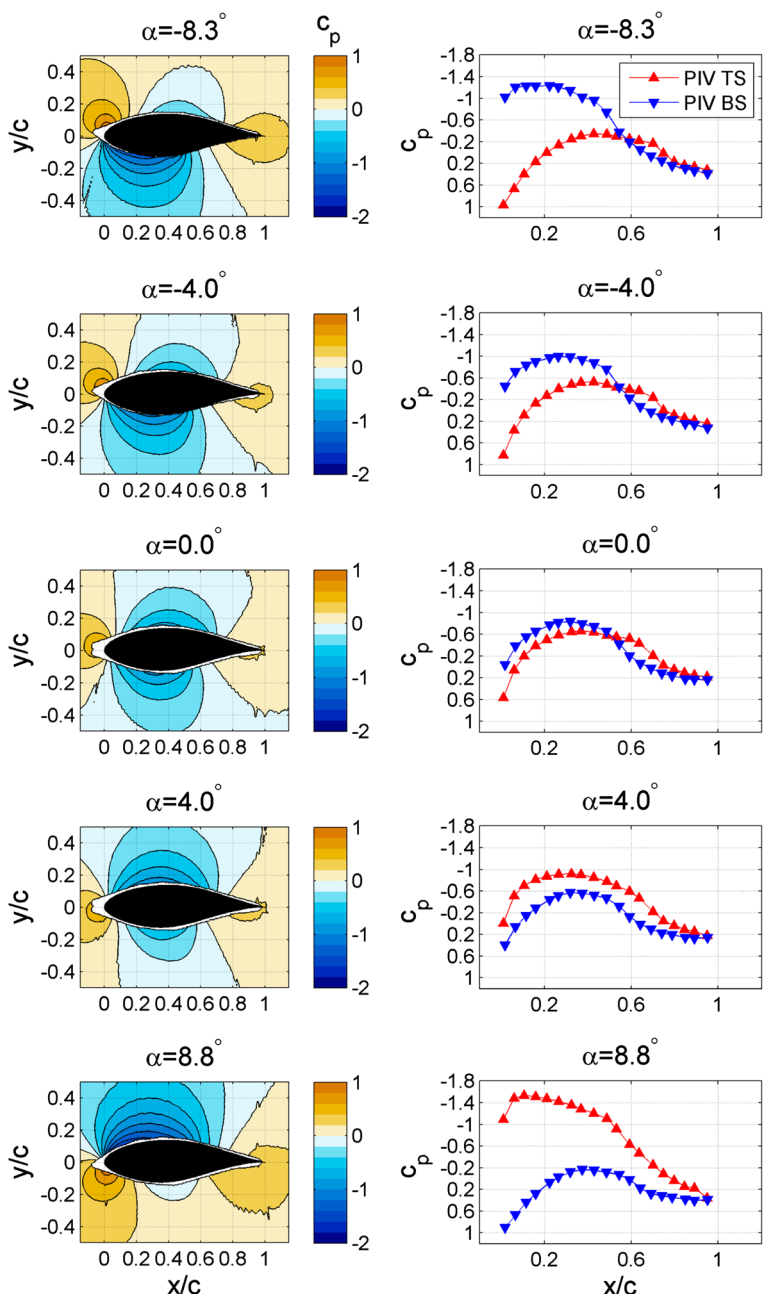


Figure 15. PIV pressure coefficient distribution (airfoil frame of reference, airfoil straight, flow at an angle), $k = 0.104$, $v = 2.66$ Hz, $V_\infty = 20$ m s $^{-1}$.

6. EVALUATION OF THE PERFORMANCE OF THE AIRFOIL ON A 2D VAWT

Figure 17 presents the simulated power coefficient (C_P) for a three-bladed VAWT as a function of tip speed ratio (λ) and solidity for the DU12W262; the simulations are based on the experimental airfoil polar for the DU12W262 (Figures 9 and 10).

Figure 18 presents the results of the simulations for a three-bladed VAWT, plotting simulated power coefficient (C_P) as a function of tip speed ratio (λ) for the DU12W262 (numerical and experimental) and NACA 0015, NACA 0018 (numerical and experimental), NACA 0025 and NACA 0030 airfoils. The results show the DU12W262 airfoil outperforming the NACA 4-series airfoils for its range of tip speed ratios larger than the original design range ($4.5 < \lambda < 5.5$), as initially intended. An interesting result is the difference between the performance calculated for the DU12W262 with the numerical

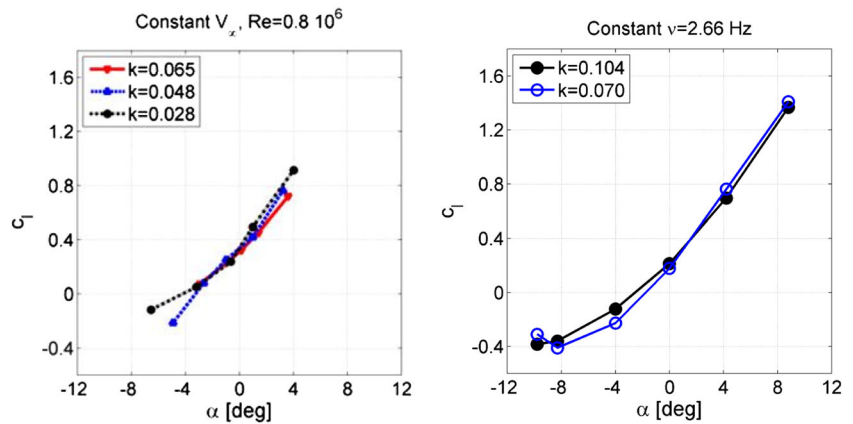
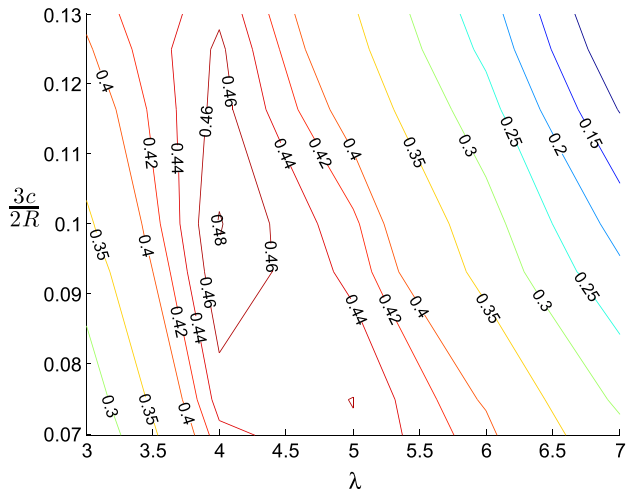


Figure 16. Unsteady loads for five cases of different reduced frequency and amplitude. Low reduced frequency, several amplitudes (left); high reduced frequency, the same amplitude (right).



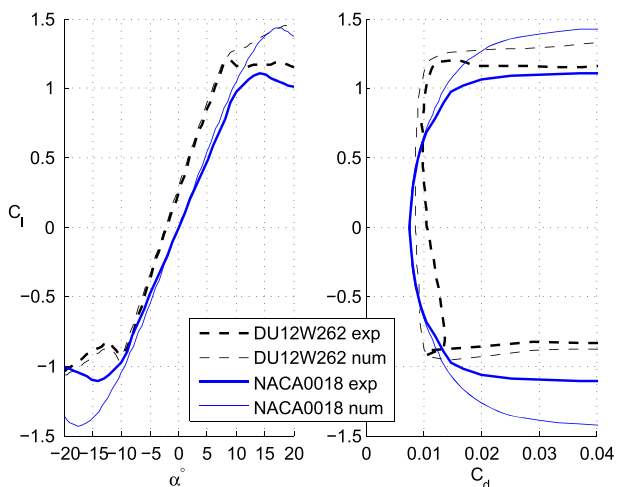


Figure 19. Numerical and experimental polars for the airfoils DU12W262 and NACA 0018 (experimental NACA 0018 data from the work of Timmer⁷).

simulation data and the experimental data. This is a result from the discrepancy between the experimental and numerical polars of the airfoil, which are a consequence of the limitations of both the numerical and the experimental simulations. These discrepancies can also be observed in the results for the experimental and numerical results for the NACA 0018 airfoil; the numerical and experimental polars of both airfoils are plotted in Figure 19.

Figure 19 shows that the discrepancies observed in Figure 18 for the two airfoils have two different origins. While for the NACA0018, the source is a difference between experimental and numerical prediction of the lift slope, in the case of the DU12W262, the discrepancy is mainly due to a higher experimental drag than predicted numerically. The difference of the results in drag for the DU12W262 is most probably a consequence of the difference between the numerically predicted transition inside a small laminar bubble for minimum drag, and a different behaviour in the experimental results; although the presence of a small separation bubble and transition can be observed in the experimental results, such a phenomena is very sensitive and can lead to smaller or larger drag values than predicted. A sensitivity analysis to drag uncertainty is presented in the work of Simão Ferreira and Geurts.¹⁵

7. CONCLUSIONS

The work aimed at testing an airfoil for VAWTs, which was designed accordingly to the objective function proposed by Simão Ferreira and Geurts.¹⁵ The designed airfoil performance has been tested for a range of Reynolds numbers of the order of 0.7 to 1 million, relevant for wind-energy applications. The experimental wind-tunnel results were served to validate numerical predictions; the numerical and experimental results matched well for the $c_l(\alpha)$ curve, but the numerical results for $c_d(\alpha)$ under-predict the experiments. As the airfoil is optimized with the use of a small separation bubble for transition, small variations between numerical and experimental models can justify this difference in drag without significant difference in lift. The results also confirm the suitability of using PIV for the study of surface pressure and loads on moving airfoils, allowing for both a full quantification of the flow field and the determination of the loads in a non-intrusive manner. The unsteady results show a clear effect of separated flow hysteresis; these experimental data are thus valuable for model validation, as they provide both velocity and pressure fields at several phases of a complex unsteady airfoil flow. The simulations using the experimental and numerical airfoil polar results showed that the new DU12W262 airfoil out-performed the NACA 4-series airfoils that were used in the initial population of the genetic optimization method from which the DU12W262 originated. The experimental work is not able to duplicate the flow curvature effect experienced by a blade section of a VAWT; future experiments of VAWT blade section in rotation are planned.

ACKNOWLEDGEMENTS

The authors would like to thank Stefan Bernardy (TU Delft) for his advice and contribution into making the experiments successful. Additionally, Ben Geurts (TU Delft), Ricardo Pereira (TU Delft), Laura Vitale (Università di Napoli), Nando Timmer (TU Delft), Matthew Barone (Sandia National Laboratories), Uwe Schmidt Paulsen (DTU Wind) and Helge Madsen (DTU Wind) are acknowledged for their advice and discussion. This work is made possible in part because of funds from Technology Foundation STW-Veni grant and Future Emerging Technologies FP7-Deepwind project.

APPENDIX: COORDINATE DU12W262

Table A.1 presents the coordinates of the DU12W262. s/c is the surface length starting from the trailing edge top-side.

Table A.1. Coordinates DU12W262. s/c is the surface length starting from the trailing edge top-side.

s/c	x/c	y/c	s/c	x/c	y/c	s/c	x/c	y/c
0.00000	1.00000	0.00052	0.94534	0.08056	0.07844	1.20847	0.11321	-0.08192
0.01650	0.98398	0.00445	0.96061	0.06689	0.07163	1.23086	0.13441	-0.08909
0.04491	0.95634	0.01103	0.97396	0.05522	0.06515	1.25592	0.15842	-0.09627
0.07692	0.92524	0.01863	0.98571	0.04523	0.05898	1.28326	0.18488	-0.10316
0.11128	0.89202	0.02738	0.99611	0.03666	0.05307	1.31221	0.21314	-0.10946
0.14731	0.85739	0.03733	1.00541	0.02929	0.04741	1.34207	0.24250	-0.11486
0.18486	0.82152	0.04842	1.01378	0.02296	0.04193	1.37223	0.27236	-0.11915
0.22377	0.78448	0.06038	1.02138	0.01753	0.03660	1.40238	0.30235	-0.12215
0.26320	0.74701	0.07262	1.02834	0.01293	0.03139	1.43238	0.33232	-0.12377
0.30183	0.71021	0.08436	1.03475	0.00907	0.02627	1.46231	0.36225	-0.12392
0.33919	0.67444	0.09516	1.04070	0.00593	0.02121	1.49235	0.39226	-0.12258
0.37531	0.63963	0.10483	1.04626	0.00348	0.01623	1.52277	0.42254	-0.11971
0.41041	0.60557	0.11329	1.05148	0.00170	0.01132	1.55387	0.45333	-0.11532
0.44471	0.57204	0.12053	1.05641	0.00056	0.00652	1.58600	0.48491	-0.10938
0.47843	0.53886	0.12653	1.06109	0.00004	0.00187	1.61953	0.51760	-0.10194
0.51175	0.50588	0.13130	1.06563	0.00014	-0.00267	1.65478	0.55171	-0.09305
0.54481	0.47301	0.13484	1.07035	0.00104	-0.00730	1.69193	0.58745	-0.08291
0.57772	0.44019	0.13717	1.07532	0.00277	-0.01196	1.73073	0.62465	-0.07189
0.61054	0.40739	0.13829	1.08060	0.00530	-0.01660	1.77012	0.66240	-0.06067
0.64331	0.37461	0.13822	1.08624	0.00856	-0.02121	1.80899	0.69976	-0.04992
0.67600	0.34195	0.13697	1.09232	0.01252	-0.02582	1.84706	0.73651	-0.03995
0.70853	0.30951	0.13456	1.09893	0.01721	-0.03047	1.88437	0.77268	-0.03084
0.74074	0.27749	0.13104	1.10615	0.02266	-0.03521	1.92085	0.80823	-0.02262
0.77239	0.24617	0.12647	1.11412	0.02896	-0.04008	1.95615	0.84277	-0.01535
0.80312	0.21594	0.12094	1.12298	0.03623	-0.04515	1.98964	0.87568	-0.00915
0.83249	0.18727	0.11460	1.13292	0.04464	-0.05046	2.02070	0.90634	-0.00420
0.85999	0.16066	0.10765	1.14418	0.05441	-0.05605	2.04908	0.93451	-0.00072
0.88520	0.13653	0.10033	1.15704	0.06582	-0.06198	2.07500	0.96037	0.00108
0.90784	0.11515	0.09290	1.17181	0.07918	-0.06828	2.09911	0.98447	0.00090
0.92783	0.09655	0.08555	1.18885	0.09487	-0.07493	2.11470	1.00000	-0.00052

REFERENCES

- Akimoto H, Tanaka K, Uzawa K. Floating axis wind turbines for offshore power generation—a conceptual study. *Environ. Res. Lett.* 2011; **6**(044017). DOI: 10.1088/1748-9326/6/4/044017.
- Paquette J, Barone M. Innovative offshore vertical-axis wind turbine rotor project. *EWEA 2012 Annual Event*, Copenhagen Denmark, 2012.
- Paulsen US, Vita L, Madsen HA, Hattel J, Ritchie E, Leban KM, Berthelsen PA, Carstensen S. 1st deepwind 5MW baseline design. *Energy Procedia* 2012; **24**(0): 27–35.
- Sutherland HJ, Berg DE, Ashwill TD. A retrospective of vawt technology. *Sandia Report SAND2012-03044*, Sandia National Laboratories, Livermore, CA, 2012.
- Jamieson P. *Innovation in Wind Turbine Design*. John Wiley & Sons: The Atrium, Southern Gate, Chichester, West Sussex, United Kingdom, 2011.
- Sheldahl RE, Klimas PC. Aerodynamic characteristics of seven symmetrical airfoil sections through 180-degree angle of attack for use in aerodynamic analysis of vertical axis wind turbines. *Technical Report SAND81-2114*, Sandia National Laboratories, 1981.
- Timmer W. Two-dimensional low-Reynolds number wind tunnel results for airfoil NACA 0018. *Wind Engineering* 2008; **32**(6): 525–537.
- Klimas PC. Tailored airfoils for vertical axis wind turbines. *Technical Report SAND84-1062*, Sandia National Laboratories and United States. Dept. of Energy, 1984.
- Galbraith R, Coton F, Dachun J. Aerodynamic design of vertical axis wind turbines. *Technical Report GU Aero 9246*, University of Glasgow, 1992.

10. Claessens M. The design and testing of airfoils for application in small vertical axis wind turbines. *Master's Thesis*, Faculty of Aerospace Engineering, Delft University of Technology, 2006.
11. Sullivan W. Economic analysis of Darrieus vertical axis wind turbine systems for the generation of utility grid electric power - vol. 2: the economic optimization model. *Technical Report*, Sandia National Laboratories, 1979.
12. Jiang D, Coton F, Galbraith RM. A fixed vortex model for vertical axis wind turbines including unsteady aerodynamics. *Wind Engineering* 1991; **15**(6): 348–360.
13. Basuno B, Coton F, Galbraith R. A prescribed wake aerodynamic model for vertical axis wind turbines. *Proceedings of the Institution of Mechanical Engineers, Part A: Journal of Power and Energy* 1992; **206**: 159–166. Available at: http://www.researchgate.net/publication/245391667_A_prescribed_wake_aerodynamic_model_for_vertical_axis_wind_turbines.
14. Coton F, Jiang D, Galbraith R. Unsteady prescribed wake model for vertical axis wind turbines. *Proceedings of the Institution of Mechanical Engineers, Part A: Journal of Power and Energy* 1994; **208**: 13–16. Available at: <http://pia.sagepub.com/content/208/1/13.full.pdf>.
15. Simão Ferreira C, Geurts B. Aerofoil optimisation for the vertical axis wind turbine. *submitted to Wind Energy* 2013. Available at: <http://onlinelibrary.wiley.com/doi/10.1002/we.1762/abstract>.
16. Wilson RE. Vortex sheet analysis of the Giromill. *Journal of Fluids Engineering* 1978; **100**(3): 340–342.
17. Coene R. Elements of the aerodynamic theory of cyclogyro wing systems with concentrator effects. *Technical Report LR-338*, Delft University of Technology - Aerospace faculty.
18. Madsen HA. On the ideal and real energy conversion in a straight bladed vertical axis wind turbine. *Technical Report*, Institute of Industrial Constructions and Energy Technology-Aalborg University Centre, 1983.
19. Madsen HA. The actuator cylinder: a flow model for the vertical axis wind turbine. *Proceedings of the 7th British Wind Energy Association Conference*, Aalborg University Centre, Denmark, 1985; 147–154.
20. Simão Ferreira C. The near wake of the vawt: 2D and 3D views of the VAWT aerodynamics, *Ph.D. Thesis*, Delft University of Technology, 2009. ISBN/EAN:978-90-76468-14-3.
21. Simão Ferreira C, Scheurich F. Demonstrating that power and instantaneous loads are decoupled in a vertical axis wind turbine. *Wind Energy* 2013. Available at: <http://onlinelibrary.wiley.com/doi/10.1002/we.1581/abstract>.
22. de Oliveira G. Wind turbine airfoils with boundary layer suction, a novel design approach, *Master's Thesis*, Delft University of Technology, 2011.
23. van Oudheusden B, Scarano F, Roosenboom E, Casimir E, Souverein L. Evaluation of integral forces and pressure fields from planar velocimetry data for incompressible and compressible flows. *Experiments in Fluids* 2007. Available at: <http://link.springer.com/article/10.1007%2Fs00348-007-0261-y>.
24. Ragni D, van Oudheusden B, Scarano F. 3D pressure imaging of an aircraft propeller blade-tip flow by phase-locked stereoscopic PIV. *Experiments in Fluids* 2012; **52**: 463–477.
25. van Oudheusden B. PIV-based pressure measurement. *Measurement Science and Technology* 2013; **24**(3). Available at: <http://iopscience.iop.org/0957-0233/24/3/032001>.
26. Westerweel J. Digital particle image velocimetry, *Ph.D. Thesis*, Delft University of Technology, 1993.
27. Elsinga G, van Oudheusden B, Scarano F. Evaluation of aero-optical distortion effects in PIV. *Experiments in Fluids* 2005; **39**(2): 245–256.
28. Schrijer F, Scarano F. Particle slip compensation in steady compressible flows. *7th International Symposium on Particle Image Velocimetry*, Rome, Italy, 2007; 1–6.
29. Schrijer F, Scarano F. Effect of predictor-corrector filtering on the stability and spatial resolution of iterative piv interrogation. *Experiments in Fluids* 2008; **45**: 927–941.
30. Braslow AL, Knox EC. Simplified method for determination of critical height distributed roughness particles for boundary-layer transition at Mach numbers from 0 to 5. *NACA TN 4363*, 1958.
31. Allen H. Wall interference in a two-dimensional flow wind tunnel with consideration of the effect of compressibility. *NACA*, 1944.
32. Acum WEA, Garner HC, Maskell EC, Rogers EWE, Subsonic wind tunnel wall corrections Advisory Group for Aerospace Research and Development (North Atlantic Treaty Organisation). *Technical Report AGARD-AG-109*, 1966.

SUPPORTING INFORMATION

Additional supporting information may be found in the online version of this article at the publisher's web-site.